A Comparative Study of the Cubic-Plus-Association Equation of State and a Peng-Robinson Equation of StatefiBased Solid Model for Asphaltene Simulation in the Wellbore

Fernando M. C. Coelho[1]*, Ryosuke Okuno[1], Kamy Sepehrnoori[1], and Ofodike A. Ezekoye[1]

[1]The University of Texas at Austin

Summary

Asphaltene is one of the main flow-assurance concerns in oil production. Its precipitation and further deposition along the flow path (wellbore or reservoir) can cause reduced hydrocarbon flow rates and even a total blockage. These potential damages have caused a growing interest in computationally efficient methods to predict asphaltene precipitation, depending on flow conditions.

This paper presents two different approaches: (*i*) a model from Li and Firoozabadi (2010), using a simplified version of the cubic-plus-association equation of state (CPA EOS), and (*ii*) a version of a solid model based on the Peng-Robinson (PR) EOS, with no association term. The two approaches are compared in isolated flash calculations and wellbore flow simulations with asphaltene deposition. The comparisons are made using the same fluid parameters for both approaches as much as possible.

Results show that, if provided with adequate input data, the solid model can consistently match results from the more complex CPA model quite successfully for several fluid compositions. An attempt is made to explain the "success" of the solid model in reproducing CPA model results. The solid model cannot adjust to fluid-composition changes in a manner similar to that of CPA. Therefore, the solid model seems more suitable for wellbore than reservoir simulation, which tends to involve a higher level of fluid mixing. However, the efficiency of the solid model can reduce the computational time by a factor of 2 in comparison with CPA.

Introduction

Asphaltenes are a class of hydrocarbons defined by solubility criteria. They compose the fraction of petroleum insoluble in normal alkanes (e.g., heptane) but soluble in aromatics (e.g., toluene). Together with saturates, aromatics, and resins, asphaltenes make one of the four classes measured by the SARA analysis, widely used to characterize a given crude oil. Asphaltenes are typically associated with complex, heteroatomic molecules containing multiple aromatic rings—highly polar and amorphous (noncrystalline). Asphaltene molecular weight has been the subject of enduring discussions as the molecules aggregate even at low concentrations in good solvents and may form clusters of six to eight molecules (Vargas and Tavakkoli 2018). Unlike wax (or paraffin), which appears when the fluid temperature drops below a certain threshold, asphaltene precipitation is usually a pressure-driven process in the wellbore. With decreasing pressure along the flow, the oil swells because of the expansion of the light fractions. Asphaltenes are insoluble in these light hydrocarbons, making the oil a poor solvent. As a result, asphaltenes precipitate. The oleic phase shows the least solubility for these molecules at the bubblepoint. If depressurization continues, an increasingly larger fraction of light components moving to the gas phase makes the remaining oil more aromatic. Redissolution is then an expected output as pressure decreases below the bubblepoint. Like other deposits, its buildup to the pipe walls can decrease flow rates. Common remediation measures are mechanical removal and/or aromatic solvent injection (e.g., xylene).

According to Vargas and Tavakkoli (2018), the average cost associated with asphaltene in the Gulf of Mexico, for example, is around USD 70 million per well if a shut-in is required. Due to the relevance of asphaltene issues in oil production, its prediction is therefore of great importance. The different methods could be classified into two main groups—one that considers asphaltenes and oil to form a true solution (the solubility models) and another that asphaltenes are insoluble yet stabilized in oil by resin-like molecules (the colloidal models). The latter is out of the scope of this work. The first group comprises all methods using thermodynamic relations to predict asphaltene precipitation through conventional liquid-liquid or solid-liquid equilibria. For that, cubic EOSs can be used. A straightforward approach—called here the solid models—assumes that asphaltene precipitates as a single pseudocomponent in the solid phase, while the oil and gas phases are modeled with a cubic EOS. Examples of solid models can be found in Gupta (1986), Thomas et al. (1992), and Nghiem et al. (1993). Alternatively, more advanced methods may include the association between different molecules. Among them is the use of CPA and statistical associating fluid theory (SAFT) EOSs.

The CPA EOS was initially developed to model species with hydrogen bonds (Kontogeorgis et al. 1996; Kontogeorgis and Folas 2009), which often exhibit complicated thermodynamic behavior. The Soave-Redlich-Kwong (SRK) EOS (Soave 1972) was combined with an association term from the more complex SAFT EOS (Chapman et al. 1990), based on the perturbation theory. Li and Firoozabadi (2009) then used the PR EOS (Peng and Robinson 1976) for the physical interactions (thus replacing SRK) of water-containing mixtures. Since asphaltenes are the most polar fraction of petroleum and show an associative nature, the same authors extended the idea by modeling the self-association of the asphaltene fraction and cross-association of the asphaltene and heavy pseudocomponents (Li and Firoozabadi 2010). They successfully reproduced the experiments for the onset pressures and the amount of precipitated asphaltene for several live oils, induced by a pressure decrease or CO_2 mixing. Later, Nasrabadi et al. (2016) presented the corresponding equation framework. Inspired by Li and Firoozabadi (2010), Arya et al. (2015) proposed to study asphaltenes with a version of CPA based on SRK EOS and were also able to correlate onset experimental data with a relatively simple model. Similarly, Jia and Okuno (2018) used an SRK/CPA

---

*Corresponding author; email: fernando.coelho@utexas.edu

Original SPE manuscript received for review 16 May 2022. Revised manuscript received for review 23 August 2022. Paper (SPE 212293) peer approved 26 August 2022.

model to study the multiphase behavior from cross-association of water and asphaltene in reservoir fluids, such as heavy oil or bitumen, which could lead to the formation of an asphaltene-rich emulsion phase.

Although there has been growing attention to CPA for asphaltene applications, an alternative is using the entire SAFT theory, not just the derived association term. After its original release by Chapman et al. (1990), Gross and Sadowski (2001) developed the perturbed-chain SAFT (PC-SAFT) EOS, in which the chain-length dependence of the attractive (dispersive) interactions is also considered. Because of the similarity of asphaltenes to large-size, heavy molecules, PC-SAFT has also been tested successfully to predict the phase behavior of this petroleum fraction. However, beyond the obvious advantage of CPA being partly based on conventional cubic EOSs (thus making fluid characterization easier), Zhang et al. (2012) compared the performance of CPA with PC-SAFT for asphaltene modeling and reached the conclusion of a slight advantage in favor of CPA. When using PC-SAFT, they reported not being able to find a suitable set of parameters to fit experimental onset points for a few of the tested fluids, contrary to CPA. A similar remark was made by Arya et al. (2016a) after comparing CPA with two versions of PC-SAFT, those being with and without association. Whereas CPA and PC-SAFT with association correlated the upper onset boundary for all six fluids in their work (Arya et al. 2016a), PC-SAFT without association was unable to do the same for two of the fluids. Conversely, Nascimento et al. (2019) concluded that PC-SAFT with association is better than CPA, claiming that PC-SAFT is more accurate for onset calculations outside the experimental temperature range.

This paper compares the results from one of the proposed CPA/asphaltene models in the literature (Li and Firoozabadi 2010) with a solid model. To the best of our knowledge, it is the first time such a comparison has been made. Abouie et al. (2017) did a similar one, only between PC-SAFT and a solid model derived from the work of Nghiem et al. (1993). In their work, a good agreement is claimed between the results of the PC-SAFT and solid models with experimental data. Their results showed that both models predicted asphaltene in the wellbore with a similar trend but distinct deposit thicknesses. According to the authors, the asphaltene mole fraction changed as deposition occurred, and the solid model was not able to adapt. In this research, we reproduce some of the flash results from Li and Firoozabadi (2010) with CPA, alongside those generated with a modified solid model, also based on Nghiem et al. (1993). Both models are described, and an attempt is then made to justify the similarities/differences. We also extend the comparison to wellbore flow simulations, considering the formation of asphaltene deposits.

Model Development

This section describes the two models used in this research to predict asphaltene precipitation: the CPA approach from Li and Firoozabadi (2010) and a version of a solid model based on the PR EOS.

CPA Model. The CPA EOS, proposed by Kontogeorgis et al. (1996), can be expressed in terms of pressure (P), composed of physical and association contributions, as follows:

$$P = P^{\text{physical}} + P^{\text{association}}, \tag{1}$$

$$P^{\text{association}} = -\frac{1}{2}\frac{RT}{v}\left(1 - v\frac{\partial \ln g}{\partial v}\right)\sum_{i} x_i \sum_{A_i}\left(1 - X_{A_i}\right), \tag{2}$$

where v is the molar volume, R is the gas constant, T is the temperature, g is the radial distribution function, x_i is the molar fraction of the component i, and X_{A_i} represents the fraction of sites A on molecule i that do not form bonds with other active sites.

We implement the CPA EOS following Li and Firoozabadi (2010). Accordingly, we use the PR EOS for the physical part; self-association is considered for the asphaltene fraction only, and cross-association exclusively between the asphaltene and the heavy component (HC). The radial distribution function is approximated by the pure hard-sphere fluid as $g = \left(1 - 0.5\eta\right) / \left(1 - \eta\right)^3$, with $\eta = b/4v = B/4Z$.

For a particular phase, the compressibility factor (Z) can be found by solving

$$Z = \frac{Z}{Z - B} - \frac{AZ}{Z^2 + 2BZ - B^2} - \frac{1}{2}\left(\frac{1 + \eta - 0.5\eta^2}{1 - 1.5\eta + 0.5\eta^2}\right)\left[N_a x_a\left(1 - X_a\right) + N_{HC} x_{HC}\left(1 - X_{HC}\right)\right], \tag{3}$$

where N_i is the number of association sites per molecule i, $A = aP/(RT)^2$, and $B = bP/RT$. If $x_a = 0$ (no asphaltene), Eq. 2 reduces to the PR EOS, from which come the definitions of parameters a and b come. Furthermore,

$$X_a = \frac{Z}{Z + \left(\dfrac{P}{RT}\right)\left(N_a x_a X_a \Delta^{aa} + N_{HC} x_{HC} X_{HC} \Delta^{aHC}\right)}, \tag{4}$$

$$X_{HC} = \frac{Z}{Z + \left(\dfrac{P}{RT}\right) N_a x_a X_a \Delta^{aHC}}, \tag{5}$$

where $\Delta^{ij} = g\left(\eta\right) k_{ij} b_{ij}\left[\exp\left(\varepsilon_{ij}/RT\right) - 1\right]$ $\left(i = a;\ j = a, HC\right)$ represents the association strength; $b_{ij} = \left(b_i + b_j\right)/2$ is the averaged b parameter; and k_{ij} and ε_{ij} are the association volume and energy parameters, respectively.

The fugacity coefficient (ϕ_i) is given as follows:

$$\begin{aligned}\ln\phi_i = {} & \frac{b_i}{b}\left(\frac{B}{Z - B} - \frac{AZ}{Z^2 + 2BZ - B^2}\right) - \ln\left(Z - B\right) - \frac{A}{2\sqrt{2}B}\left(\frac{2\sum_{j=1}^{n_c} x_j a_{ij}}{a} - \frac{b_i}{b}\right)\ln\left(\frac{Z + \left(1 + \sqrt{2}\right)B}{Z + \left(1 - \sqrt{2}\right)B}\right) \\ & - \frac{B}{8Z}\left(\frac{2.5 - \eta}{1 - 1.5\eta + 0.5\eta^2}\right)\left[N_a x_a\left(1 - X_a\right) + N_{HC} x_{HC}\left(1 - X_{HC}\right)\right] + N_i \ln X_i,\end{aligned} \tag{6}$$

with $N_i = 0,\ i \neq a, HC$.

Newton's method is initially applied to find Z with the corresponding value from the cubic EOS (the PR EOS, in this case) as the initial guess. The so-needed derivatives can be found in Nasrabadi et al. (2016) and, also, here in Appendix A with a few corrections. If a root cannot be found, a bisection algorithm is used subsequently. The nonbonded fractions X_a and X_{HC} are calculated via successive substitution with an initial guess of 0.5. These calculations are part of an iterative loop with an overall tolerance of 10^{-7}. Asphaltene precipitation is then identified by the appearance of a stable second-liquid hydrocarbon phase, predominantly composed of asphaltene. For the flash calculation, we use the framework developed by Perschke (1988) with only a few modifications: (*i*) For phase identification, as in Mohebbinia (2013: p. 85–87), we label the phase with the highest mole fraction of the heaviest component (i.e., asphaltene) as the second-liquid (asphaltene-rich) phase; (*ii*) for the stability analysis of a trial phase, we use all the $n_c + 4$ initial estimates recommended by Li and Firoozabadi (2012), where n_c is the total number of components of a given hydrocarbon mixture; and (*iii*) successive substitution only is used in both the phase-stability and phase-split calculations.

Solid Model. As the name suggests, this model assumes asphaltene precipitates as a pure solid if favorable conditions arise. It relies on any component showing the same fugacity ($f_i = \phi_i x_i P$) throughout all the phases. Hence, the asphaltene component has the same fugacity (f_a) across the liquid, vapor, and solid (Eq. 7):

$$f_a^L = f_a^V = f_a^S. \tag{7}$$

While the asphaltene fugacity in the oil and gas phases is calculated directly from the cubic EOS, the corresponding value for the pure solid is based on the previous knowledge of the onset pressure P^* at a given temperature T. Immediately below this pressure P^*, solid asphaltene is expected to precipitate. For the point (P^*, T), the fugacity of the solid is assumed equal to the fugacity of the asphaltene component calculated by the EOS via flash calculation at (P^*, T). For any other pressure P, the solid phase fugacity at the same temperature T can be corrected by the Poynting factor (Sandler 1994, p. 370) as follows:

$$\ln\left(f_a{}^S\big|_{P,T}\right) = \ln\left(f_a{}^S\big|_{P^*,T}\right) + \frac{1}{RT}\int_{P^*}^{P} v_a^S \, dP. \tag{8}$$

Assuming constant molar volume for the solid asphaltene (v_a^S), we obtain, as in Nghiem et al. (1993):

$$\ln\left(f_a{}^S\big|_{P,T}\right) = \ln\left(f_a{}^S\big|_{P^*,T}\right) + v_a^S\frac{(P - P^*)}{RT}. \tag{9}$$

Hence, to consider asphaltene precipitation at given conditions (P, T), we

1. Perform a flash at the asphaltene onset pressure P^* to obtain the fugacity of the asphaltene component ($f^L_{aP^*,T}$), given by the EOS, at the onset condition.
2. Assume the solid asphaltene fugacity $f^S_{aP^*,T} = f^L_{aP^*,T}$.
3. Calculate the fugacity of the solid asphaltene at the given conditions ($f^S_{aP,T}$) using Eq. 9.
4. Perform another flash, this time at pressure P, to calculate the fugacity of the asphaltene component in the fluid mixture at the given conditions ($f^L_{aP,T}$).
5. If $f^L_{aP,T} > f^S_{aP,T}$, precipitation should occur. Otherwise, this procedure stops.
6. Solve a Rachford-Rice equation, Eq. 10, for the liquid/solid system (assuming asphaltene in the gas is negligible):

$$\sum_{i=1}^{n_c} \frac{x_i\left(1 - K_i^{SL}\right)}{1 - \beta\left(1 - K_i^{SL}\right)} = 0, \tag{10}$$

   where x_i is the normalized mole fraction of component i in the liquid/solid system; β is the normalized mole fraction of the solid phase; $K_i^{SL} = 0$ if $i \neq a$; and $K_a^{SL} = \phi_a^L/\phi_a^S$ with $\phi_a^S = f_a^S/P$ (Pedersen et al. 2015, p. 291).
7. The previous step estimates the solid (asphaltene) mole fraction of the liquid/solid system. With this, we recalculate the liquid composition, and another flash is performed to update ϕ_a^L and K_a^{SL}.
8. Go back to Step 6 if the solid mole fraction is not converged.
9. Finally, we obtain the amount of asphaltene precipitate to satisfy mole balance and the fugacity constrain from Eq. 7.

The previous method is the same as outlined in Abouie et al. (2016) but for one main difference: We lump both liquid phases whenever a second liquid is identified. Because we run a three-phase flash algorithm for the hydrocarbon phases, we notice the persistent occurrence of a second liquid while using the same fluid characterization shown in Li and Firoozabadi (2010). This is the case even when using the PR EOS alone (i.e., without the association term). If not for the lumping procedure, the solid asphaltene calculation would be compromised with severe discontinuities. The reason not to perform a two-phase flash instead is to avoid missing the gas phase by only keeping the two liquids. This issue is to be detailed in the following sections.

For both models, if volume-shift (Peneloux) parameters are used, the compressibility factor and fugacity coefficients from Eqs. 3 and 6, respectively, are corrected in the following manner for each fluid phase:

$$Z_{\text{Pen}} = Z - \frac{cP}{RT}, \tag{11}$$

$$\ln \phi_{i_{\text{Pen}}} = \ln \phi_i - \frac{c_i P}{RT}, \tag{12}$$

where $c = \sum_i x_i c_i$ and $c_i = VSP_i \, b_i$.

Analysis

This section compares the asphaltene-related results generated by the two models outlined in the previous section.

Fluid Characterization. We replicate some of the calculations performed by Li and Firoozabadi (2010) with the fluid compositions shown in **Table 1,** which contains the explicit amounts of the heavy and asphaltene pseudocomponents. For simplicity, all the pseudocomponents are hereafter referred to as just "components."

	Fluid X1	Fluid X2	Fluid X3	Fluid Y3
N_2	0.09	0.27	0.38	0.47
CO_2	1.02	4.07	4.02	1.59
H_2S	0.05			1.44
C1	42.41	30.53	46.07	32.22
C2	10.78	7.13	7.72	12.42
C3	6.92	5.92	5.62	10.29
*i*C4	1.55	2.43	1.14	2.03
*n*C4	2.92	1.11	2.35	4.87
*i*C5	1.47	0.82	0.75	2.22
*n*C5	1.82	0.79	0.67	2.71
C6	2.86	1.36	0.82	4.12
C7		2.67	1.03	
C8		3.82	1.58	
C9		4.17	1.91	
C10		4.07	0.79	
Heavy comp. (HC)	28.09	30.56	24.98	25.48
Asphaltene	0.02	0.28	0.17	0.14

Table 1—Composition of the live oils (mol%).

For CPA, just like Li and Firoozabadi (2010), we adopt $N_a = N_{HC} = 4$, $k_{aa} = k_{aHC} = 0.01$, and $\varepsilon_{aa}/R = 3,600°R$. The asphaltene component is characterized the same throughout all the fluids in **Table 1**, with $MW_a = 1{,}800$ lb/lbmol, which makes it the heaviest component. The necessary parameters for phase equilibria (e.g., critical properties, acentric factor, molecular weight, and binary interaction coefficients) can be found in Li and Firoozabadi (2010) and, also, in Appendix B for the sake of completeness (Tables B-1 through B-4). To the best of our knowledge, the only difference lies in the cross-association energy parameter for the heavy component (HC) of Fluid X3. Instead of the three discrete values used in their paper, we regress an expression (Eq. 13) to be used between 86 and 266°F:

$$\varepsilon_{aHC}/R = 0.0048\,T^2 - 6.941\,T + 5028.1, \tag{13}$$

where T is the temperature in °R. This is done to allow the wellbore simulations in the following sections.

For the solid model, we replicate the same fluid characterization used for CPA as much as possible (Tables B-1 through B-3 in Appendix B). Consequently, we take a different approach from Nghiem et al. (1993), Shirdel (2013), and Abouie et al. (2016). In their research, the heaviest component in the oil phase is assumed to split into nonprecipitating (heavy) and precipitating (asphaltene) components. Properties of the two (e.g., critical properties and acentric factors) are identical, except for the binary interaction coefficients with lighter components. Here, the asphaltene and heavy components do not share the same parameters. Additionally, for the molar volume of the solid asphaltene (v_a^S in Eq. 9), we attempt to bring some physical meaning by using a correlation from Barrera et al. (2013), based on the molecular weight of asphaltene (MW_a). From Eq. 14, if $MW_a = 1{,}800$ lb/lbmol, then $v_a^S = 25.4$ ft^3/lbmol. The cited works (Nghiem et al. 1993; Shirdel 2013; Abouie et al. 2016) have considered the v_a^S parameter as a tuning factor, spanning from 10.3 to 20.7 ft^3/lbmol:

$$v_a^S = \frac{16.0185\,MW_a}{1100 + 100\left(1 - \exp\left(-\frac{MW_a}{3850}\right)\right)}. \tag{14}$$

Flash Results. Starting with Fluid X1, **Fig. 1** shows the experimental points for both upper and lower asphaltene onset pressures across several temperatures and the corresponding bubblepoint data. The solid lines represent the result of the CPA modeling by Li and Firoozabadi (2010). Generally, they show a good agreement with the data points, especially for the upper onset and bubblepoints. The lower onset results show a moderate deviation. Also shown in the figure is the result from the solid model (dashed lines). As can be seen, it performs similarly to CPA. Note that the upper onset points are not calculated for the solid model. They are among the necessary inputs for the model, as already explained in the previous section. In this case **(Fig. 1)**, the experimental pressures are then used as input. The lower onset points predicted by the solid model are remarkably similar to CPAs. There is one clear outlier among the experimental upper onset points at 241°F. Had it been disregarded as input for the solid model, results from both models for the lower onset line would have been even closer. Nevertheless, we keep it to show the corresponding effect on the solid-model result: a slightly decreased lower onset pressure (at 241°F) than CPA. Appendix C contains the experimental data (Tables C-1 through C-3) and corresponding references used in this paper.

For Fluid X2 at 86°F, the fraction of precipitated asphaltene as a function of pressure is depicted in **Fig. 2.** Data points are from experiments. The lines are the results from the CPA and solid models. This time, the upper onset pressure for the solid model, a necessary input, is assumed equal to the one calculated by CPA (7,588 psi). Both models show very close results when considering volume-shift

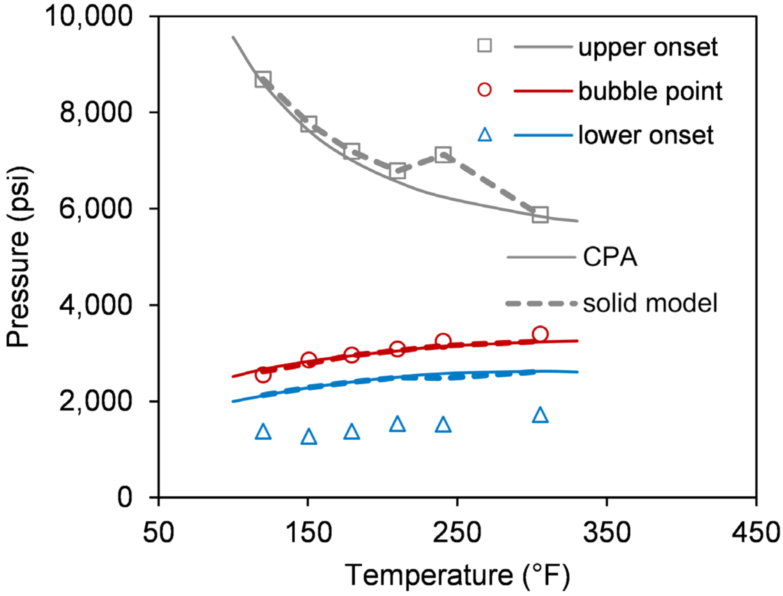

Fig. 1—Asphaltene onset and bubblepoint pressures as a function of temperature for Fluid X1. Data points are from experiments, and lines are calculated.

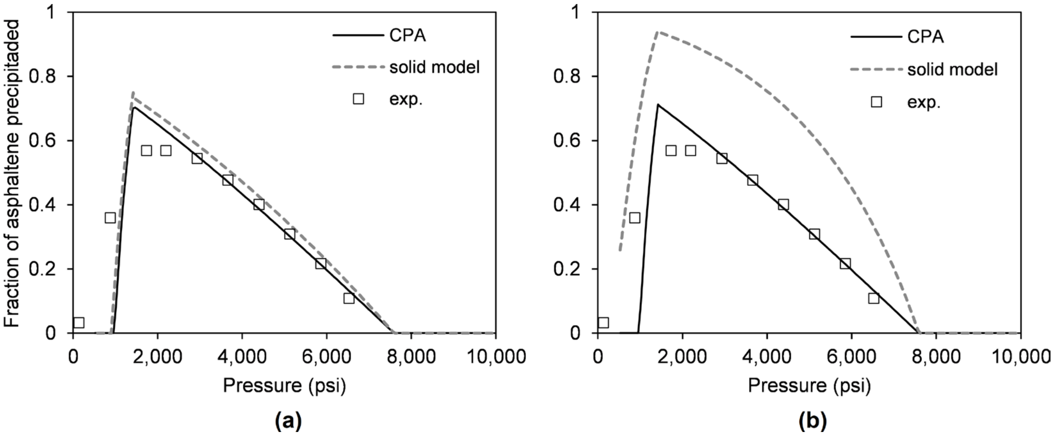

Fig. 2—Precipitated asphaltene as a function of pressure for Fluid X2 at 86°F. Data points are from experiments, and lines are from our simulations. Results are (a) with and (b) without volume shift.

parameters **(Fig. 2a)**. However, without volume shift **(Fig. 2b)**, the solid model's results change significantly, whereas CPAs remain unchanged. For the CPA model, phase mole fractions are not affected by volume shift (parameters for each component are shown in Appendix B). For the solid model, the fraction of precipitated asphaltene varies because volume shift affects the EOS-based fugacity (at the onset pressure P^*), while the solid asphaltene mole volume (v_a^S) is kept constant regardless of volume-shift consideration in Eq. 9.

In **Fig. 3,** a similar conclusion can be drawn. Again, after using CPA-calculated upper onset pressures as input for the solid model, both show a close agreement when predicting the fraction of precipitated asphaltene for Fluid X3 at three distinct temperatures. Only the results with volume shift are demonstrated. Experimental results are not shown in the figure for the sake of clarity.

Solid-Model Justification. The similarity between the CPA and solid models shown above suggests that modeling the fluid behavior with the PR EOS alone may already provide reasonable results. For all the fluids in **Table 1**, a second-oil phase can also be found with the PR EOS. For example, the closest results compared with CPA are for Fluid Y3, as seen in **Fig. 4.** While the lower onset lines and bubblepoint pressures for the CPA and PR EOSs show a very good agreement, the upper lines are just slightly off.

Similarly, for Fluid X2, a second-oil phase is also present when modeling fluid behavior through the PR EOS alone. Its composition, together with CPAs, is shown in **Fig. 5** after a flash at a pressure (1,400 psi) immediately below the bubblepoint at 86°F. For the heavy component, cross-association with asphaltene when using CPA causes its fraction in the corresponding second-oil phase to be more significant than that of the PR EOS alone (about double). That is the most relevant difference; for all the other components, the fractions are similar, including asphaltene. Assuming such a high molecular weight for the asphaltene component (MW_a = 1,800 lb/lbmol) seems to have induced the appearance of an asphaltene-rich phase even without association.

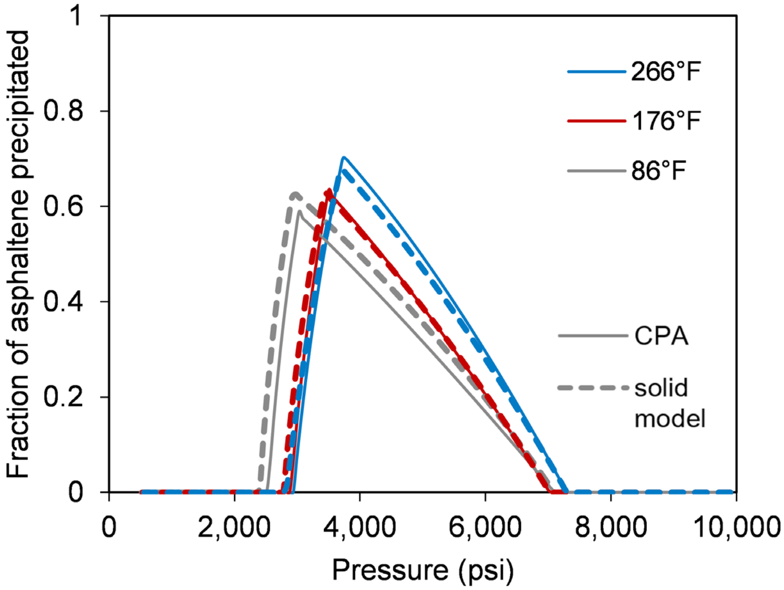

Fig. 3—Precipitated asphaltene as a function of pressure for Fluid X3 at three different temperatures: 86, 176, and 266°F—comparison between the CPA and solid models.

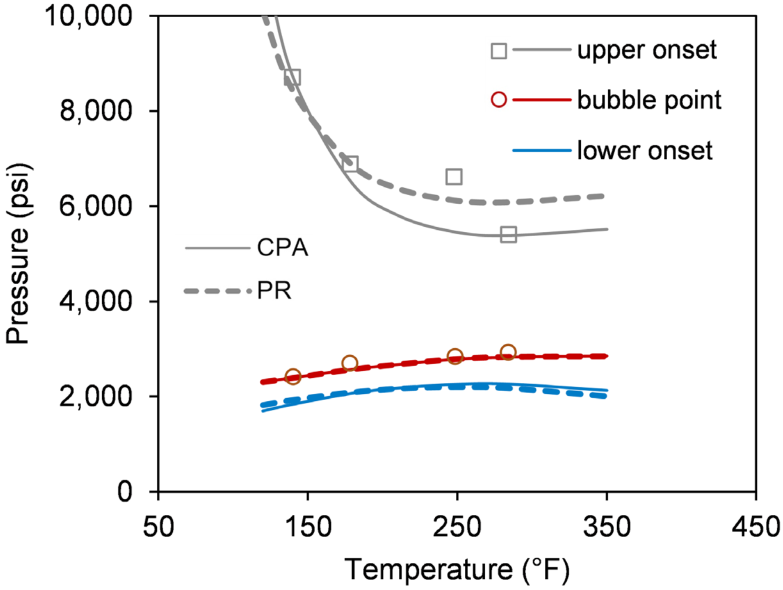

Fig. 4—Asphaltene onset and bubblepoint pressures as a function of temperature for Fluid Y3. Data points are from experiments, and lines are calculated.

The results shown in **Figs. 4 and 5** suggest that the solid model, as described in the initial section, provides a fine adjustment to the already-reasonable results by the PR EOS alone, in terms of the amount of precipitated asphaltene.

Deposition Study. More than only standalone flash calculations, we compare the CPA and solid models when they are used for comprehensive flow simulations in the wellbore, with the possibility of asphaltene deposits building upon the walls. For this, we use UTWELL, a 1D thermal compositional simulator (Shirdel 2013; Abouie 2019; Coelho et al. 2021a, 2021b). Besides handling the multiphase flow in the wellbore, it also has capabilities related to scales, wax, asphaltenes, and hydrates. Appendix D gives a brief description of the steady-state flow models in UTWELL.

As the solid model relies on onset pressures to be provided in advance (as input) for a particular fluid composition, we wanted to verify how it performs when part of the precipitated asphaltene is left behind in the form of a deposit on the tubing walls. In such a situation, the solid model is constrained to the same inputs, whereas CPA would theoretically lead to new onset pressures (upper and lower) as the total fluid composition varies. The idea is to check if the solid model's results are compromised, compared with CPA's, because of this inherent

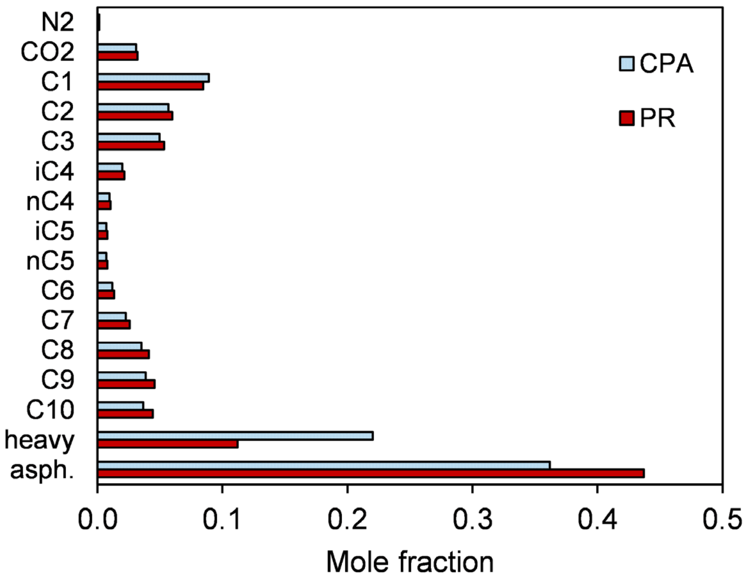

Fig. 5—Second-oil phase composition for Fluid X2 at 1,400 psi and 86°F.

limitation. UTWELL is then configured to run both the CPA and solid models, as detailed previously. We set up a synthetic case **(Table 2)** based on the conditions of petroleum production off the coast of Brazil. Moreover, we use the same fluid as before (Fluid X3), only with lumped components to speed up the simulation. The fluid-characterization parameters are then taken as molar averages from the original Fluid X3.

Well and Reservoir Data		Fluid Data	
		Component	Mole Fraction (%)
Bottomhole depth	16,500 ft	CO_2	4.02
Reservoir temperature	150°F	N_2+C1	46.45
Reservoir pressure	8,000 psi	C2	7.72
Topside pressure	500 psi	C3	5.62
Liquid productivity index	75 STB/psi·D	C4-C5	4.91
Overall heat transfer coefficient	2.8 BTU/ft^2·hr·°F	C6-C10	6.13
Net pay zone	100 ft	Heavy	24.98
Tubing inside diameter	6 in.	Asphaltene	0.17
Water cut	0%		

Table 2—Case study definition. Composition is for Fluid X3 with lumped components.

We consider the transport of asphaltene particles from the bulk fluid toward the wall and subsequent adhesion to the surface using an Arrhenius-type expression for the sticking probability factor. The deposited asphaltene is assumed to have a uniform thickness along a particular cross section. Also included is the removal of deposited asphaltene by shear forces in the wellbore. These mechanisms were thoroughly detailed by Shirdel et al. (2012); some of the equations are also described in Appendix D for the sake of completeness. More important for this research's goals is that the corresponding inputs (Shirdel 2013, p. 208–211) are kept constant when running the cases with the CPA and solid models to allow for a straightforward comparison.

Before any asphaltene is deposited on the walls, **Fig. 6** shows that the pressure, temperature, and liquid-holdup profiles from both models match quite well for the initial timestep. Moreover, the total mass-flow rate difference between the two lies below 1%. Then, after a 90-day simulation, **Fig. 7** shows a deposit growing by the middle of the wellbore. Results are for the deposit thickness (δ) relative to the internal radius of the tubing (r_i). It starts building up as soon as asphaltenes first precipitate, and it develops until the flowing pressure achieves the lower onset point. Below such pressure, asphaltene no longer precipitates, as the oil phase entirely redissolves it. The location of the maximum deposit thickness tends to coincide with that of the maximum precipitated asphaltene in the fluid, about where its bubblepoint pressure is reached. As the deposit thickness increases with time, the available flow area is reduced; so is the total flow rate from the well. The imposed boundary conditions—constant reservoir and topside pressures—make the bubblepoint pressure occur increasingly deeper in the well as the simulation continues. Therefore, the point of maximum thickness tends to move down the wellbore with time.

In terms of the required computational time, the solid model runs considerably faster than CPA. As **Fig. 8** shows, it takes about half the total time to run the 90-day simulation with the solid model compared with CPA. Nonetheless, both models show very similar results

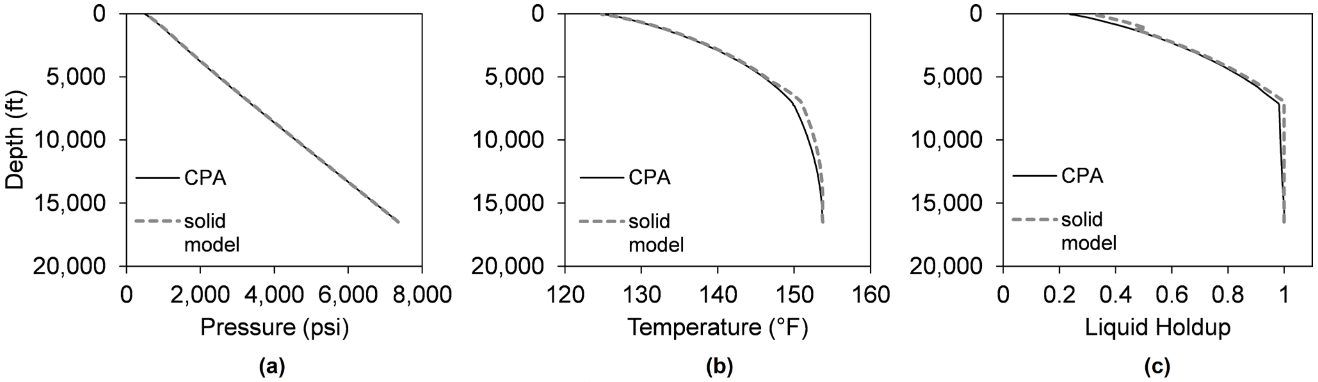

Fig. 6—(a) Pressure, (b) temperature, and (c) liquid-holdup profiles for the initial timestep. Comparison between the CPA and solid models.

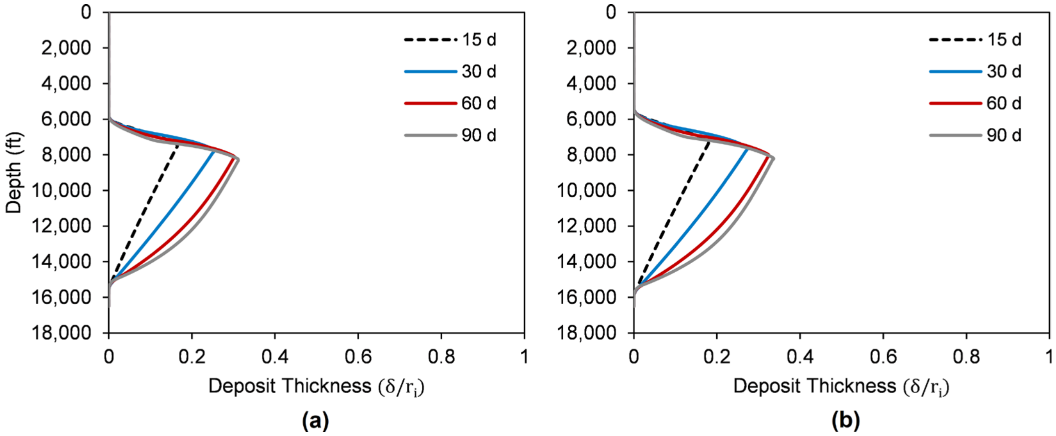

Fig. 7—Relative thickness of asphaltene deposits after a 90-day simulation with (a) CPA and (b) the solid model.

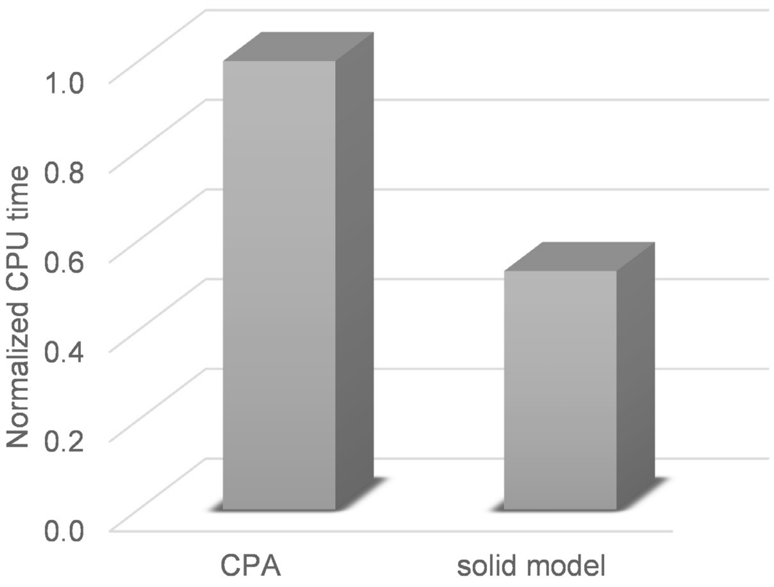

Fig. 8—Computational-time comparison between the CPA and solid models[i].

---

[i] While the simulation takes 2.94 hours with CPA, the solid model requires only 1.56 hours. Both are run with the same 169 gridblocks, 120 timesteps, and CPU—Intel® Xeon®, 3.5 GHz, four cores, and 16-GB RAM.

in developing the asphaltene deposits **(Fig. 7)**. This is achieved not only because of the results alike in terms of the fraction of precipitated asphaltene **(Fig. 3)** but also because of the assumption that it is only pure asphaltene that deposits, regardless of the model. Furthermore, despite the solid model using a correlation (Barrera et al. 2013) for the fixed density of pure asphaltene, the resulting value (70.87 lb/ft^3) is well within the range of the calculated value for pure asphaltene with CPA across the wellbore (from 70.79 to 70.94 lb/ft^3, for the initial timestep). Such agreement is lost if the volume-shift parameters are disabled (73.8 lb/ft^3, on average, with CPA), as in **Fig. 2** for Fluid X2.

The previous results are achieved considering asphaltene precipitation as a totally reversible process (i.e., the precipitated asphaltene can be redissolved if thermodynamically indicated). Another possibility is to consider some conversion of the reversible asphaltene into a flocculated (or irreversible) form, according to Eqs. 15 and 16 (Shirdel 2013, p. 146–148):

$$\frac{d\left[C_{s2}\right]}{dt} = k\left[C_{s1}\right], \tag{15}$$

$$\left[C_{s1}\right] = \left[C_{s1}\right]_0 \, e^{-kt}, \tag{16}$$

where $\left[C_{s1}\right]$ and $\left[C_{s2}\right]$ are the concentrations of the reversible and irreversible forms of asphaltene, in lbmol/ft^3, respectively, and k is a constant. In this case, flocculated asphaltenes would not be redissolved even if the thermodynamic equilibrium indicates so. **Fig. 9** shows the deposit profile in the wellbore after 90 days of simulation for three different conditions: Asphaltene is totally reversible (k = 0, same as in **Fig. 7**), partial conversion to an irreversible form (k = 0.001), and also at a conversion rate such that all precipitated asphaltene can effectively be considered as irreversible (k = 1). Once again, the results are very similar for both the CPA and solid models. One crucial difference is that, for CPA, the irreversible asphaltenes are considered inert and, as such, do not take part in the flash calculation. Meanwhile, for the solid model, the flocculated (or irreversible) asphaltenes are still considered for the equilibrium (i.e., they contribute to the mole fraction of the asphaltene component used in the flash). After the flash calculation, the mole flow rate of flocculated asphaltenes is then restored.

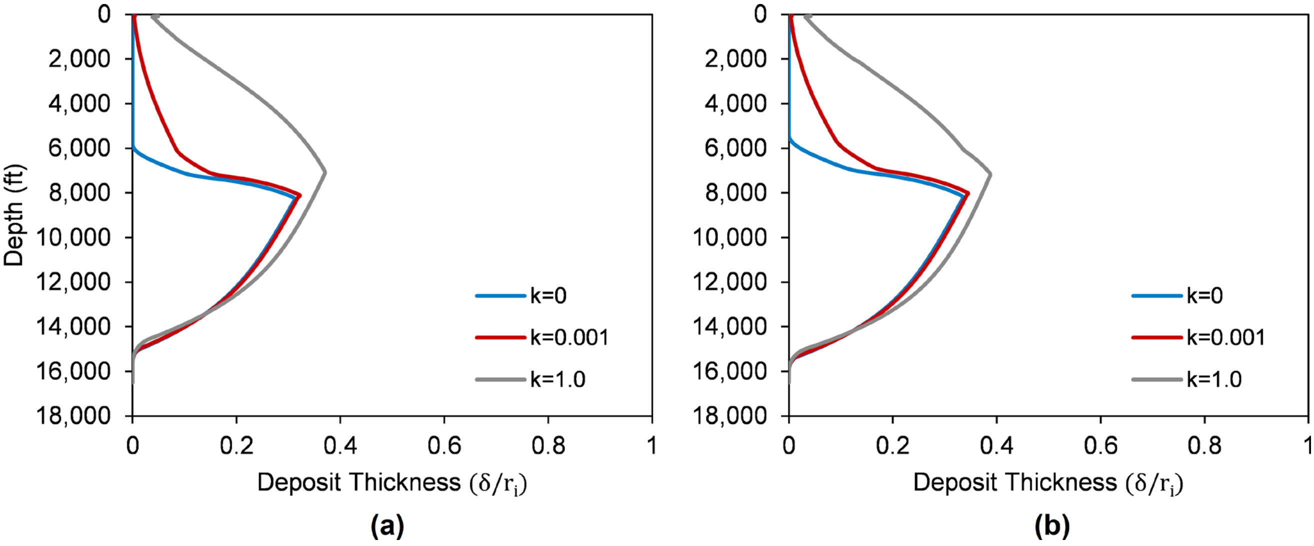

Fig. 9—Deposit profiles after a 90-day simulation for when asphaltene is totally reversible (*k* = 0), gets partially converted to irreversible (*k* = 0.001), and totally irreversible (*k* = 1)—results with (a) CPA and (b) the solid model.

Up to this point, results with the CPA and the solid models are remarkably close, regardless of the reversibility assumption. Abouie et al. (2017) expressed that the solid model is not able to adapt to the changing asphaltene mole fraction as deposition occurs along the flow because of the fixed onset input; however, this limitation did not compromise the solid model's results when compared with CPAs.

We further verify the solid model when the composition changes are more significant in the wellbore without corresponding onset data. We then rerun the cases from **Fig. 7** considering a constant gas lift injection just above the perforations, without any other changes to the inputs for both models. Conditions of the gas lift injection are according to **Table 3.** For the initial timestep, the constant gas flow rate represents about 5 wt% of the total flow rate coming from the reservoir. Gas is injected into the wellbore as a mass source; this isolates the impact of composition changes on asphaltene precipitation. In reality, a localized temperature drop would be expected, with a combined effect on asphaltenes.

Well Data		Fluid Data	
		Component	Mole Fraction (%)
Mandrel depth	13,000 ft	CO_2	5
		N_2+C1	75
Gas lift flow rate	15 MMscf/D	C2	10
		C3	10

Table 3—Gas lift system definition.

The results, with asphaltene as totally reversible only, are depicted in **Fig. 10** and show a clear difference in the shape of the deposit, depending on the model. At the gas lift mandrel depth (marked by a dotted line in the figure), an abrupt increase in the thickness of the asphaltene deposit can be observed for both models. Such an increase is significantly more pronounced when using CPA. Furthermore, after 90 days of simulation, the total mass flow rate using the solid model is 43% higher than with CPA. This can be easily justified while comparing the flash results before and after mixing with gas in **Fig. 11.** First, for CPA, the pressure range at which asphaltene is expected to precipitate increases dramatically. Interestingly, the lower onset pressure remains almost the same as before mixing. Even though no experimental results are available to support these results, this is the expected behavior after adding a poor asphaltene solvent (like the gas from **Table 3**) to the original fluid—Arya et al. (2016b) studied the effect of gas injection on asphaltene precipitation and reached similar conclusions with experimental data. In **Fig. 10a**, despite the high deposition rate, the maximum deposit thickness barely changes from the 30th day onward due to a shear removal process at a similar rate. Then, for the solid model, the upper onset pressure remains unchanged in **Fig. 11** (of course, since no new onset pressures are provided), and the lower onset pressure increases. As a result, the region where asphaltene precipitates is reduced, contrary to the expected behavior. The slight increase in the deposit thickness, seen at the gas injection location in **Fig. 10b**, is only the result of the minor increase seen in the fraction of precipitated asphaltene after "jumping" from the premixed to the mixed curve **(Fig. 11)** before the bubblepoint is reached.

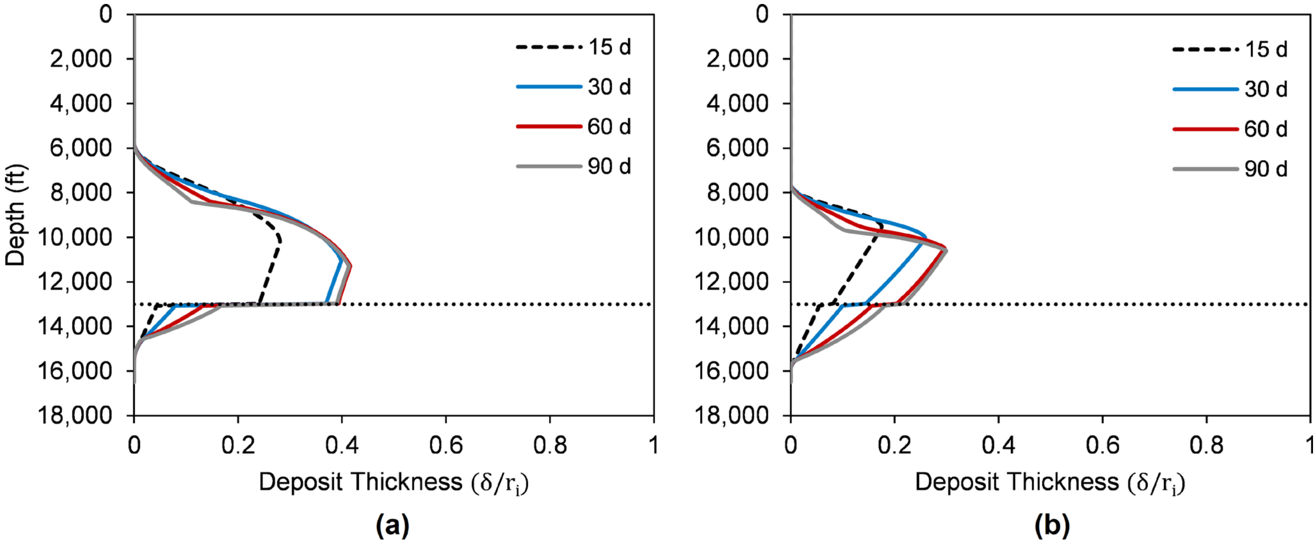

Fig. 10—Relative thickness of asphaltene deposits after a 90-day simulation with (a) CPA and (b) the solid model. The dotted line indicates the position of the gas lift injection (where mixing occurs).

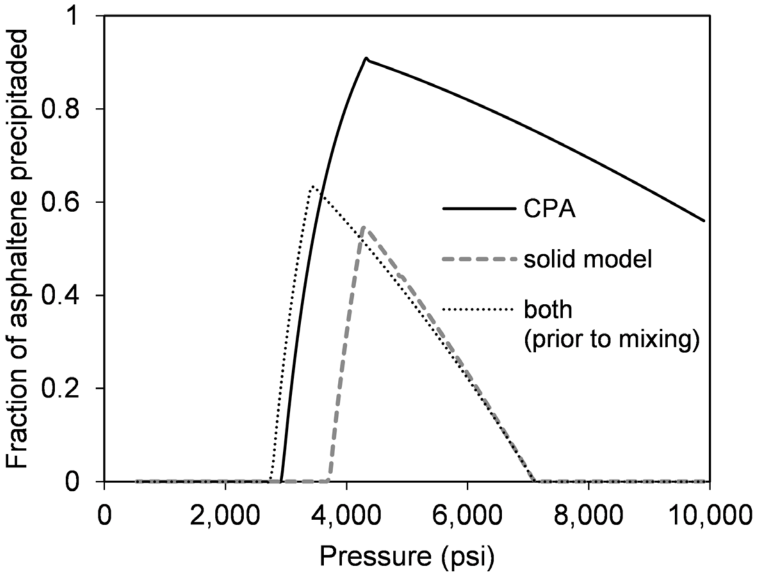

Fig. 11—Precipitated asphaltene as a function of pressure for the lumped fluid X3 at 176°F. Comparison between the CPA and solid models before (dotted line) and after (solid and dashed lines) mixing with gas.

As seen above, an obvious disadvantage of the solid model is the need to provide upper onset pressures in advance, particularly when fluid mixing occurs. While the CPA model can adapt to a new composition, the solid model would need new input data. Nevertheless, this issue could be circumvented by interpolating lookup tables for different mixing ratios, if available. This inherent limitation of the solid model—dependent on a comprehensive set of asphaltene onset pressures for any fluid composition that might occur—seems to make its implementation more promising for simulations in the wellbore, rather than in the reservoir. For a fixed composition, the need of onset input is not necessarily a disadvantage of the solid model compared with CPA, since the latter also relies on such data for prior regression of its parameters, most notably the energy parameters ε_{ij}.

Summary and Conclusions

The following are the conclusions of this study:

1. A modified solid model gave similar results of asphaltene precipitation in comparison with CPAs, at least for the approach adopted by Li and Firoozabadi (2010). This was confirmed not just for isolated flash calculations but also for wellbore simulations with asphaltene deposition.
2. Even though providing similar results, the solid model was considerably faster than CPA—about half the time needed by the latter for the case tested.
3. The success of the solid model in matching the CPA model's results seems to be connected to how Li and Firoozabadi (2010) chose to model the asphaltene component in their work. If the PR EOS alone is used with their original fluid-characterization scheme (i.e., only without the association term), an asphaltene-rich phase is still likely to occur, with onset pressures relatively close to the experimental data. The addition of the association term from CPA then moves the results even closer. It is shown here that the same effect is achieved via a modified solid model, without the complexities coming from CPA EOS.
4. A disadvantage of the solid model is the need to provide upper onset pressures in advance. This is particularly critical when fluid mixing occurs, as shown in one of the case studies (with gas lift, results in **Fig. 10**). While the CPA model copes with it theoretically, the solid model would need new onset data corresponding to the new mixture composition. Nevertheless, this issue could be circumvented by interpolating lookup tables with onset pressures for different mixing ratios (if such data are available, of course).
5. Even if out of the scope of this work, a better understanding of asphaltene deposition and removal processes is needed, especially for multiphase flow. The models used here are based on experiments of solid particles in a single-phase flow (either gas or liquid). Therefore, we encourage further research into this area, potentially providing new models and parameters to asphaltene deposition/removal depending on the flow regimes.

Nomenclature

A = flow section area
C_i = concentration of the species i
D = pipe diameter
f = friction factor
f_i = fugacity of the component i
g = gravity
g_c = unit conversion factor
h_k = enthalpy of phase k
$\dot{H}_k$ = enthalpy influx term of phase k
J_c = unit conversion factor
k_{ij} = association volume parameter between molecules i and j
K_D = deposition coefficient
$\dot{m}_d$ = deposited particle mass flux
MW_i = molecular weight of component i
N_i = number of association sites per molecule i
P = pressure
P_{ci} = critical pressure of the component i
$\dot{Q}_{\text{loss}}$ = heat exchange per unit length
Q_k = volumetric flow rate of phase k
r_i = internal radius
R = gas constant
SP = sticking probability
S_p = stopping distance of a particle
t = time
t_p = relaxation time of a particle
T = temperature
T_{ci} = critical temperature of the component i
u_k = velocity of phase k
v = molar volume
V_{b_I} = volume of the gridblock I
V_p = particle velocity
VSP_i = volume-shift parameter of the component i
x = distance
X_{A_i} = fraction of sites A on molecule i that do not form bonds with other active sites
x_i = molar fraction of component i
Z = compressibility factor
α_k = volumetric fraction of phase k

β = normalized mole fraction of the solid phase in the liquid/solid system
Γ_k = mass transfer term of phase k
δ = deposit thickness
Δ^{ij} = association strength between molecules i and j
ε_{ij} = association energy parameter between molecules i and j
θ = inclination angle
μ = viscosity
ρ_k = density of phase k
τ = wall shear stress
φ_i = fugacity coefficient of the component i
$\dot{\psi}_k$ = mass influx term of phase k

Acknowledgments

This work was supported by the Brazilian Petroleum Corporation—PETROBRAS—and by the Reservoir Simulation Joint Industry Project at the Center for Subsurface Energy and the Environment of The University of Texas at Austin.

References

Abouie, A. 2019. *Development of an Integrated Compositional Wellbore-Reservoir Simulator for Flow Assurance Problems*. PhD Dissertation, University of Texas at Austin, Austin, Texas, USA. https://doi.org/10.26153/tsw/13507.

Abouie, A., Korrani, A. K. N., Shirdel, M. et al. 2017. Comprehensive Modeling of Scale Deposition by Use of a Coupled Geochemical and Compositional Wellbore Simulator. *SPE J.* **22** (4): 1225–1241. SPE-185942-PA. https://doi.org/10.2118/185942-PA.

Abouie, A., Rezaveisi, M., Mohebbinia, S. et al. 2016. Static and Dynamic Comparison of Equation of State Solid Model and PC-SAFT for Modeling Asphaltene Phase Behavior. Paper presented at the SPE Western Regional Meeting, Anchorage, Alaska, USA, 23–26 May. SPE-180480-MS. https://doi.org/10.2118/180480-MS.

Arya, A., Von Solms, N., and Kontogeorgis, G. M. 2015. Determination of Asphaltene Onset Conditions Using the Cubic plus Association Equation of State. *Fluid Ph Equilibria* **400**: 8–19. https://doi.org/10.1016/j.fluid.2015.04.032.

Arya, A., Liang, X., Von Solm, N. et al. 2016a. Modeling of Asphaltene Onset Precipitation Conditions with Cubic Plus Association (CPA) and Perturbed Chain Statistical Associating Fluid Theory (PC-SAFT) Equations of State. *Energy Fuels* **30** (8): 6835–6852. https://doi.org/10.1021/acs.energyfuels.6b00674.

Arya, A., Von Solms, N., and Kontogeorgis, G. M. 2016b. Investigation of the Gas Injection Effect on Asphaltene Onset Precipitation Using the Cubic-Plus-Association Equation of State. *Energy Fuels* **30** (5): 3560–3574. https://doi.org/10.1021/acs.energyfuels.5b01874.

Barrera, D. M., Ortiz, D. P., and Yarranton, H. W. 2013. Molecular Weight and Density Distributions of Asphaltenes from Crude Oils. *Energy Fuels* **27** (5): 2474–2487. https://doi.org/10.1021/ef400142v.

Bird, R. B., Stewart, W. E., and Lightfoot, E. N. 2002. *Transport Phenomena*, second edition. New York, USA: John Wiley & Sons.

Buenrostro-Gonzalez, E., Lira-Galeana, C., Gil-Villegas, A. et al. 2004. Asphaltene Precipitation in Crude Oils: Theory and Experiments. *AIChE J* **50** (10): 2552–2570. https://doi.org/10.1002/aic.10243.

Chapman, W. G., Gubbins, K. E., Jackson, G. et al. 1990. New Reference Equation of State for Associating Liquids. *Ind Eng Chem Res* **29** (8): 1709–1721. https://doi.org/10.1021/ie00104a021.

Coelho, F. M. C., Sepehrnoori, K., and Ezekoye, O. A. 2021a. Coupled Geochemical and Compositional Wellbore Simulators: A Case Study on Scaling Tendencies under Water Evaporation and CO_2 Dissolution. *J Pet Sci Eng* **202**: 108569. https://doi.org/10.1016/j.petrol.2021.108569.

Coelho, F. M. C., Sepehrnoori, K., and Ezekoye, O. A. 2021b. A Coupled Hydrate and Compositional Wellbore Simulator: Understanding Hydrate Inhibition from Associated Brines in Oil and Gas Production. *SPE Prod & Oper* **36** (4): 858–872. SPE-206716-PA. https://doi.org/10.2118/206716-PA.

Epstein, N. 1988. Particulate Fouling of Heat Transfer Surfaces: Mechanisms and Models. In *Fouling Science and Technology, NATO ASI Series*, eds. L. F. Melo, T. R. Bott, and C. A. Bernardo, 143–164. Dordrecht, The Netherlands: Springer. https://doi.org/10.1007/978-94-009-2813-8_10.

Escobedo, J. and Mansoori, G. A. 1995. Asphaltene and Other Heavy-Organic Particle Deposition During Transfer and Production Operations. Paper presented at the SPE Annual Technical Conference and Exhibition, Dallas, Texas, USA, 22–25 October. SPE-30672-MS. https://doi.org/10.2118/30672-MS.

Fahim, M. A. 2007. Empirical Equations for Estimating ADE of Crude Oils. *Pet Sci Technol* **25** (7): 949–965. https://doi.org/10.1080/10916460500526981.

Friedlander, S. K. and Johnstone, H. F. 1957. Deposition of Suspended Particles from Turbulent Gas Streams. *Ind Eng Chem* **49** (7): 1151–1156. https://doi.org/10.1021/ie50571a039.

Gross, J. and Sadowski, G. 2001. Perturbed-Chain SAFT: An Equation of State Based on a Perturbation Theory for Chain Molecules. *Ind Eng Chem Res* **40** (4): 1244–1260. https://doi.org/10.1021/ie0003887.

Gupta, A. K. 1986. *A Model for Asphaltene Flocculation Using an Equation of State*. MS Thesis, University of Calgary, Calgary, Alberta, Canada. https://doi.org/10.11575/PRISM/21686.

Hasan, A. R., Kabir, C. S., and Sayarpour, M. 2007. A Basic Approach to Wellbore Two-Phase Flow Modeling. Paper presented at the SPE Annual Technical Conference and Exhibition, Anaheim, California, USA, 11–14 November. SPE-109868-MS. https://doi.org/10.2118/109868-MS.

Jia, W. and Okuno, R. 2018. Modeling of Asphaltene and Water Associations in Petroleum Reservoir Fluids Using Cubic-plus-Association EOS. *AIChE J* **64** (9): 3429–3442. https://doi.org/10.1002/aic.16191.

Kaya, A. S., Sarica, C., and Brill, J. P. 1999. Comprehensive Mechanistic Modeling of Two-Phase Flow in Deviated Wells. Paper presented at the SPE Annual Technical Conference and Exhibition, Houston, Texas, USA, 3–6 October. SPE-56522-MS. https://doi.org/10.2118/56522-MS.

Kontogeorgis, G. M. and Folas, G. K. 2009. *Thermodynamic Models for Industrial Applications*. New York, USA: John Wiley & Sons. https://doi.org/10.1002/9780470747537.

Kontogeorgis, G. M., Voutsas, E. C., Yakoumis, I. V. et al. 1996. An Equation of State for Associating Fluids. *Ind Eng Chem Res* **35** (11): 4310–4318. https://doi.org/10.1021/ie9600203.

Li, Z. and Firoozabadi, A. 2009. Cubic-plus-Association Equation of State for Water-Containing Mixtures: Is "Cross Association" Necessary? *AIChE J* **55** (7): 1803–1813. https://doi.org/10.1002/aic.11784.

Li, Z. and Firoozabadi, A. 2010. Cubic-Plus-Association Equation of State for Asphaltene Precipitation in Live Oils. *Energy Fuels* **24** (5): 2956–2963. https://doi.org/10.1021/ef9014263.

Li, Z. and Firoozabadi, A. 2012. General Strategy for Stability Testing and Phase-Split Calculation in Two and Three Phases. *SPE J.* **17** (4): 1096–1107. SPE-129844-PA. https://doi.org/10.2118/129844-PA.

Mohebbinia, S. 2013. *Advanced Equation of State Modeling for Compositional Simulation of Gas Floods*. PhD dissertation, University of Texas at Austin, Austin, Texas, USA.

Nascimento, F. P., Costa, G. M. N., and Vieira de Melo, S. A. B. 2019. A Comparative Study of CPA and PC-SAFT Equations of State to Calculate the Asphaltene Onset Pressure and Phase Envelope. *Fluid Ph Equilibria* **494**: 74–92. https://doi.org/10.1016/j.fluid.2019.04.027.

Nasrabadi, H., Moortgat, J., and Firoozabadi, A. 2016. New Three-Phase Multicomponent Compositional Model for Asphaltene Precipitation during CO_2 Injection Using CPA-EOS. *Energy Fuels* **30** (4): 3306–3319. https://doi.org/10.1021/acs.energyfuels.5b02944.

Nghiem, L. X., Hassam, M. S., Nutakki, R. et al. 1993. Efficient Modelling of Asphaltene Precipitation. Paper presented at the SPE Annual Technical Conference and Exhibition, Houston, Texas, USA, 3–6 October. SPE-26642-MS. https://doi.org/10.2118/26642-MS.

Pedersen, K. S., Christensen, P. L., and Shaikh, J. A. 2015. *Phase Behavior of Petroleum Reservoir Fluids*, second edition. Boca Raton, USA: CRC Press, Taylor & Francis Group. https://doi.org/10.1201/b17887.

Peng, D. Y. and Robinson, D. B. 1976. A New Two-Constant Equation of State. *Ind Eng Chem Fund* **15** (1): 59–64. https://doi.org/10.1021/i160057a011.

Perschke, D. R. 1988. *Equation of State Phase Behavior Modeling for Compositional Simulation*. PhD dissertation, University of Texas at Austin, Austin, Texas, USA.

Sandler, S. I. 1994. *Models for Thermodynamic and Phase Equilibria Calculations*. New York, USA: Marcel Dekker.

Shirdel, M. 2013. Development of a Coupled Wellbore/Reservoir Simulator for Damage Prediction and Remediation. Paper presented at the SPE Annual Technical Conference and Exhibition, San Antonio, Texas, USA, 8–10 October. SPE-160914-STU. https://doi.org/10.2118/160914-STU.

Shirdel, M., Paes, D., Ribeiro, P. et al. 2012. Evaluation and Comparison of Different Models for Asphaltene Particle Deposition in Flow Streams. *J Pet Sci Eng* **84–85**: 57–71. https://doi.org/10.1016/j.petrol.2012.02.005.

Shoham, O. 2006. *Mechanistic Modeling of Gas-Liquid Two-Phase Flow in Pipes*. Richardson, Texas, USA: Society of Petroleum Engineers. https://doi.org/10.2118/9781555631079.

Soave, G. 1972. Equilibrium Constants from a Modified Redlich-Kwong Equation of State. *Chem Eng Sci* **27** (6): 1197–1203. https://doi.org/10.1016/0009-2509(72)80096-4.

Szewczyk, V., Thomas, M., and Behar, E. 1998. Prediction of Volumetric Properties and (Multi-) Phase Behaviour of Asphaltenic Crudes. *Rev Inst Fr Pét* **53** (1): 51–58. https://doi.org/10.2516/ogst:1998008.

Taitel, Y. and Dukler, A. E. 1976. A Model for Predicting Flow Regime Transitions in Horizontal and near Horizontal Gas-Liquid Flow. *AIChE J* **22** (1): 47–55. https://doi.org/10.1002/aic.690220105.

Taitel, Y., Barnea, D., and Dukler, A. E. 1980. Modelling Flow Pattern Transitions for Steady Upward Gas-liquid Flow in Vertical Tubes. *AIChE J* **26** (3): 345–354. https://doi.org/10.1002/aic.690260304.

Thomas, F. B., Bennion, D. B., Bennion, D. W. et al. 1992. Experimental And Theoretical Studies Of Solids Precipitation From Reservoir Fluid. *J Can Pet Technol* **31** (1). PETSOC-92-01-02. https://doi.org/10.2118/92-01-02.

Vargas, F. M. and Tavakkoli, M. 2018. *Asphaltene Deposition*. Boca Raton, Florida, USA: CRC Press. https://doi.org/10.1201/9781315268866.

Watkinson, A. P. and Epstein, N. 1970. Particulate Fouling of Sensible Heat Exchangers. Paper presented at the Fourth International Heat Transfer Conference, Versailles, France.

Zhang, X., Pedrosa, N., and Moorwood, T. 2012. Modeling Asphaltene Phase Behavior: Comparison of Methods for Flow Assurance Studies. *Energy Fuels* **26** (5): 2611–2620. https://doi.org/10.1021/ef201383r.

Appendix A— Compressibility Factor With CPA EoS

The compressibility factor (Z) using CPA EOS is found by applying Newton's method (Eq. A-1) to an initial estimate from the PR EOS:

$$Z^{(n+1)} = Z^{(n)} - f/f', \tag{A-1}$$

where

$$f(Z) = -Z + \frac{Z}{Z-B} - \frac{AZ}{Z^2+2BZ-B^2} - \frac{1}{2}\left(\frac{1+\eta-0.5\eta^2}{1-1.5\eta+0.5\eta^2}\right)\left[N_a x_a\left(1-X_a\right)+N_{HC}x_{HC}\left(1-X_{HC}\right)\right], \tag{A-2}$$

and the derivative f' can be found through

$$\frac{df}{dZ} = -1 + \frac{\partial F\left(Z\right)}{\partial Z} + \frac{\partial F\left(Z\right)}{\partial \eta}\frac{\partial \eta}{\partial Z} + \frac{\partial F\left(Z\right)}{\partial X_a}\frac{\partial X_a}{\partial Z} + \frac{\partial F\left(Z\right)}{\partial X_{HC}}\frac{\partial X_{HC}}{\partial Z}, \tag{A-3}$$

where

$$\frac{\partial F\left(Z\right)}{\partial Z} = \frac{-B}{\left(Z-B\right)^2} + \frac{A\left(Z^2+B^2\right)}{Z^2+2BZ-B^2}, \tag{A-4}$$

$$\frac{\partial F\left(Z\right)}{\partial \eta} = \frac{-\left(5+4\eta+0.5\eta^2\right)}{2\left(1-1.5\eta+0.5\eta^2\right)^2}\left[N_a x_a\left(1-X_a\right)+N_{HC}x_{HC}\left(1-X_{HC}\right)\right], \tag{A-5}$$

$$\frac{\partial \eta}{\partial Z} = -\frac{B}{4Z^2}, \tag{A-6}$$

$$\frac{\partial F\left(Z\right)}{\partial X_i} = \frac{N_i x_i}{2}\left(\frac{1+\eta-0.5\eta^2}{1-1.5\eta+0.5\eta^2}\right),\ i = a,\ HC, \tag{A-7}$$

$$\frac{\partial X_a}{\partial Z} = \frac{\partial F\left(X_a\right)}{\partial Z} + \frac{\partial F\left(X_a\right)}{\partial X_{HC}}\frac{\partial X_{HC}}{\partial Z} + \frac{\partial F\left(X_a\right)}{\partial \Delta^{aa}}\frac{\partial \Delta^{aa}}{\partial \eta}\frac{\partial \eta}{\partial Z} + \frac{\partial F\left(X_a\right)}{\partial \Delta^{aHC}}\frac{\partial \Delta^{aHC}}{\partial \eta}\frac{\partial \eta}{\partial Z}, \tag{A-8}$$

$$\frac{\partial X_{HC}}{\partial Z}=\frac{\partial F\left(X_{HC}\right)}{\partial Z}+\frac{\partial F\left(X_{HC}\right)}{\partial X_a}\frac{\partial X_a}{\partial Z}+\frac{\partial F\left(X_{HC}\right)}{\partial \Delta^{aHC}}\frac{\partial \Delta^{aHC}}{\partial \eta}\frac{\partial \eta}{\partial Z}, \tag{A-9}$$

$$\frac{\partial F\left(X_a\right)}{\partial Z}=\frac{\left(\frac{P}{RT}\right)\left(N_a x_a X_a \Delta^{aa}+N_{HC}x_{HC}X_{HC}\Delta^{aHC}\right)}{\left[Z+\left(\frac{P}{RT}\right)\left(N_a x_a X_a \Delta^{aa}+N_{HC}x_{HC}X_{HC}\Delta^{aHC}\right)\right]^2}, \tag{A-10}$$

$$\frac{\partial F\left(X_{HC}\right)}{\partial Z}=\frac{\left(\frac{P}{RT}\right)N_a x_a X_a \Delta^{aHC}}{\left[Z+\left(\frac{P}{RT}\right)N_a x_a X_a \Delta^{aHC}\right]^2}, \tag{A-11}$$

$$\frac{\partial F\left(X_a\right)}{\partial X_{HC}}=-\frac{\left(\frac{P}{RT}\right)N_{HC}x_{HC}\Delta^{aHC}Z}{\left[Z+\left(\frac{P}{RT}\right)\left(N_a x_a X_a \Delta^{aa}+N_{HC}x_{HC}X_{HC}\Delta^{aHC}\right)\right]^2}, \tag{A-12}$$

$$\frac{\partial F\left(X_{HC}\right)}{\partial X_a}=-\frac{\left(\frac{P}{RT}\right)N_a x_a \Delta^{aHC}Z}{\left[Z+\left(\frac{P}{RT}\right)N_a x_a X_a \Delta^{aHC}\right]^2}, \tag{A-13}$$

$$\frac{\partial F\left(X_a\right)}{\partial \Delta^{aa}}==-\frac{\left(\frac{P}{RT}\right)N_a x_a X_a Z}{\left[Z+\left(\frac{P}{RT}\right)\left(N_a x_a X_a \Delta^{aa}+N_{HC}x_{HC}X_{HC}\Delta^{aHC}\right)\right]^2}, \tag{A-14}$$

$$\frac{\partial F\left(X_a\right)}{\partial \Delta^{aHC}}==-\frac{\left(\frac{P}{RT}\right)N_{HC}x_{HC}X_{HC}Z}{\left[Z+\left(\frac{P}{RT}\right)\left(N_a x_a X_a \Delta^{aa}+N_{HC}x_{HC}X_{HC}\Delta^{aHC}\right)\right]^2}, \tag{A-15}$$

$$\frac{\partial F\left(X_{HC}\right)}{\partial \Delta^{aHC}}==-\frac{\left(\frac{P}{RT}\right)N_a x_a X_a Z}{\left[Z+\left(\frac{P}{RT}\right)N_a x_a X_a \Delta^{aHC}\right]^2}, \tag{A-16}$$

$$\frac{\partial \Delta^{ij}}{\partial \eta}=\frac{2.5-\eta}{(1-\eta)^4}\left[\exp\left(\frac{\varepsilon_{ij}}{RT}\right)-1\right]k_{ij}b_{ij},\quad i=a \text{ and } j=a,\ HC. \tag{A-17}$$

Appendix B—Fluid Parameters

The parameters shown in **Tables B1–B4** are the same as in Li and Firoozabadi (2010). The only exception is the cross-association energy between asphaltene and heavy component (ε_{aHC}) of Fluid X3. Additionally, we include the volume-shift (Peneloux) parameters used in this work.

Component	Critical Temperature (°R)	Critical Pressure (psi)	Acentric Factor	Molecular Weight (lb/lbmol)	Volume-Shift Parameter
N_2	227.2	491.7	0.039	28.0	–0.176
CO_2	547.5	1,069.7	0.239	44.0	–0.062
H_2S	671.8	1,296.7	0.081	34.1	–0.142
C1	343.0	667.0	0.011	16.0	–0.194
C2	549.6	706.6	0.099	30.1	–0.143
C3	665.7	616.1	0.153	44.1	–0.113
*i*C4	734.0	522.7	0.183	58.1	–0.099
*n*C4	765.2	550.6	0.199	58.1	–0.090
*i*C5	828.7	490.2	0.227	72.2	–0.070

Table B-1—Physical parameters of pseudo- and pure components.

Component	Critical Temperature (°R)	Critical Pressure (psi)	Acentric Factor	Molecular Weight (lb/lbmol)	Volume-Shift Parameter
*n*C5	845.5	488.8	0.251	72.2	–0.057
C6	913.3	436.9	0.296	86.2	0.013
C7	1,001.7	388.0	0.294	100.0	0.148
C8	1,034.6	366.1	0.418	114.0	0.120
C9	1,067.5	337.9	0.491	128.0	0.121
C10	1,110.7	312.6	0.534	142.0	0.137
Asphaltene	2,653.2	92.0	2	1,800	–0.042

Table B-1 (continued)—Physical parameters of pseudo- and pure components.

Fluid	Critical Temperature (°R)	Critical Pressure (psi)	Acentric Factor	Molecular Weight (lb/lbmol)	Volume-Shift Parameter
X1	1,298.3	217.6	0.80	208.5	0.278
X2	1,380.4	152.3	0.99	288.6	0.343
X3	1,415.9	143.6	1.11	320.7	0.337
Y3	1,241.8	227.7	1.01	276.0	–0.145

Table B-2—Physical parameters of the heavy component (HC) for all the fluids.

Fluid	C1	N_2	CO_2	H_2S
All	$0.0289 + 1.633\times10^{-4}\,MW_i$	0.1	0.15	0.1

Table B-3—Nonzero binary interaction coefficients involving any hydrocarbon component *i*.

Fluid	Cross-Association Energy (°R)
X1	$\varepsilon_{aHC}/R = -0.8835\,T + 2,360.7$
X2	$\varepsilon_{aHC}/R = 2,194.2$
X3	$\varepsilon_{aHC}/R = 0.0048\,T^2 - 6.941\,T + 5,028.1$
Y3	$\varepsilon_{aHC}/R = 2.0125\,T + 760.6$

Table B-4—Cross-association energy between asphaltene (*a*) and heavy component (*HC*). *T* is the temperature in °R.

Appendix C—Experimental Data

Tables C1–C3 give the experimental data for Fluids X1, X2, and Y3 shown in this paper **(Table 1)**. References are Fahim (2007), Szewczyk et al. (1998), and Buenrostro-Gonzalez et al. (2004), respectively.

Temperature (°F)	Upper Onset (psi)	Bubble Pressure (psi)	Lower Onset (psi)
120	8,688	2,553	1,378
151	7,760	2,857	1,276
179	7,194	2,959	1,378
210	6,788	3,089	1,537
241	7,121	3,249	1,523
305	5,874	3,394	1,726

Table C-1—Experimental data for Fluid X1 (Fahim 2007).

Pressure (psi)	Precipitated Fraction
136	0.033
873	0.360
1,732	0.570
2,194	0.569
2,933	0.544
3,662	0.477
4,392	0.401
5,126	0.309
5,855	0.217
6,524	0.109

Table C-2—Precipitated asphaltene after titration with *n*-heptane for Fluid X2 at 86°F (digitized from Szewczyk et al. 1998).

Temperature (°F)	Upper Onset (psi)	Bubble Pressure (psi)
144	8,705	2,435
178	6,884	2,620
248	6,607	2,850
284	5,398	2,941

Table C-3—Experimental data for Fluid Y3 (Buenrostro-Gonzalez et al. 2004). Onset data are based on transmitted light measurements through the live-oil sample during isothermal expansion.

Appendix D—UTWELL Simulator

UTWELL is a 1D, thermal, compositional wellbore simulator developed at the University of Texas at Austin (Shirdel 2013; Abouie et al. 2017; Coelho et al. 2021a, 2021b). The wellbore is divided into gridblocks in the flow direction, and the governing equations are solved for each one. The available boundary conditions are constant wellhead pressure, constant bottomhole pressure, and constant wellhead flow rate. Moreover, several flow regimes are included to determine the effect of wall and interface shear forces on the pressure calculation; local thermodynamic equilibrium condition is assumed for each gridblock; slip is included between the gas and liquid phases (no slip between oil and water phases). Despite also having transient models, only steady-state conditions are discussed here.

Multiphase Flow Equations. The main conservation equations are shown below for the three phases—oil, gas, and water (or aqueous phase).

Mass Conservation Equation. Mass balance equations are solved to find the velocities of each phase. To consider water evaporation/condensation, a mass-transfer term (Γ_w, negative for evaporation) is included in the mass-conservation equations for the water and gas phases (Eqs. D-1 and D-2, respectively). For the gas phase, another term is included (Γ_g) to consider mass transfer also with the oil phase (Eq. D-3):

$$\frac{\partial\left(\rho_w\alpha_w\right)}{\partial t}+\frac{1}{A}\frac{\partial\left(A\rho_w\alpha_w u_w\right)}{\partial x}=\dot{\psi}_w+\Gamma_w, \tag{D-1}$$

$$\frac{\partial\left(\rho_g\alpha_g\right)}{\partial t}+\frac{1}{A}\frac{\partial\left(A\rho_g\alpha_g u_g\right)}{\partial x}=\dot{\psi}_g+\Gamma_g-\Gamma_w, \tag{D-2}$$

$$\frac{\partial\left(\rho_o\alpha_o\right)}{\partial t}+\frac{1}{A}\frac{\partial\left(A\rho_o\alpha_o u_o\right)}{\partial x}=\dot{\psi}_o-\Gamma_g, \tag{D-3}$$

where ρ is the density (lbm/ft^3), α is the volumetric fraction, u is the velocity (ft/sec), $\dot{\psi}$ is the mass influx per volume (lbm/ft^3·sec), and Γ is the mass transfer per volume (lbm/ft^3·sec). All these variables refer to a specific phase indicated by subscripts w, g, and o for water, gas, and oil phases. Furthermore, A is the flow section area, t is the time, and x is the spatial coordinate.

The discretized versions of Eqs. D-1 through D-3, for steady-state conditions, are given by Eqs. D-4 through D-6, respectively. As depicted in **Fig. D-1**, a staggered grid is used in which junctions of the grid blocks are labeled with index i, and the center points with capitalized index I. Pressure, temperature, and phase volume fractions are calculated at the center of the gridblocks, while phase velocities at the junctions. Note that the spatial variation Δx in Eqs. D-4 through D-6 is embedded in the volume of the gridblock V_b:

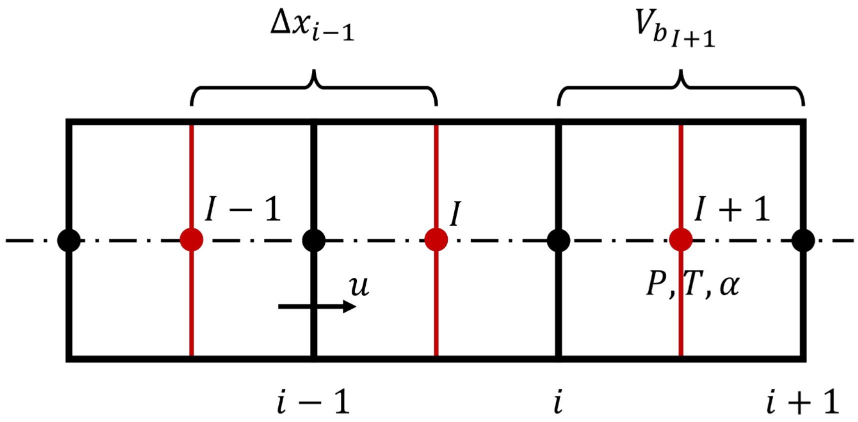

Fig. D-1—Schematic view of the staggered grid.

$$\left(\rho_w \alpha_w u_w A\right)_i - \left(\rho_w \alpha_w u_w A\right)_{i-1} = V_{b_I}\left(\dot{\psi}_{w_I} + \Gamma_{w_I}\right), \tag{D-4}$$

$$\left(\rho_g \alpha_g u_g A\right)_i - \left(\rho_g \alpha_g u_g A\right)_{i-1} = V_{b_I}\left(\dot{\psi}_{g_I} + \Gamma_{g_I} - \Gamma_{w_I}\right), \tag{D-5}$$

$$\left(\rho_o \alpha_o u_o A\right)_i - \left(\rho_o \alpha_o u_o A\right)_{i-1} = V_{b_I}\left(\dot{\psi}_{o_I} - \Gamma_{g_I}\right). \tag{D-6}$$

Momentum Conservation Equation. For the momentum balance, Eq. D-7 is solved for the mixture to find pressure and holdups. Since applying a mixture approach, no interphase mass-transfer terms are needed:

$$\frac{\partial\left(\rho_m u_m\right)}{\partial t} + \frac{\partial\left(\rho_m u_m^2\right)}{\partial x} + \left(144 g_c\right)\frac{\partial P}{\partial x} + \rho_m g \sin\theta + \frac{\tau \pi D}{A} = 0, \tag{D-7}$$

where P is the pressure (psi), τ is the wall shear stress (lbm/sec^2·ft), D is the diameter of the pipe (ft), A is the cross section of the pipe (ft^2), g is the gravity (ft/sec^2), θ is the inclination, and g_c is a unit conversion factor. The wall shear stress is calculated with

$$\tau = f\frac{\rho_m u_m^2}{8}, \tag{D-8}$$

where f is the Darcy-Weisbach friction factor.

Still in Eq. D-7, u_m and ρ_m are the velocity and density of the mixture, respectively, and are defined as

$$\rho_m = \alpha_g \rho_g + \alpha_o \rho_o + \alpha_w \rho_w, \tag{D-9}$$

$$u_m = \frac{Q_g + Q_o + Q_w}{A}. \tag{D-10}$$

Eq. D-11 is the discretized version of Eq. D-7 under steady-state conditions.

$$P_{I+1} = P_I - \Delta x_i \frac{\rho_i g \sin\theta_i}{144 g_c} - \Delta x_i \frac{f_i \rho_{m_i} u_{m_i}^2}{2 D_i \left(144 g_c A_i\right)} + \frac{\rho_{m_{I+1}}\left(u_{m_{I+1}}\right)^2 - \rho_{m_I}\left(u_{m_I}\right)^2}{144 g_c}. \tag{D-11}$$

Energy Conservation Equation. For the energy balance, the temperatures of all phases are assumed equal at each gridblock. Accordingly, Eq. D-12 is solved for the total energy conservation. Similar to the momentum balance, no interphase mass-transfer terms are needed:

$$\sum_{k=w,\ g,\ o}\left\{\frac{\partial\left[\alpha_k \rho_k\left(h_k + \dfrac{u_k^2}{2 g_c J_c}\right)\right]}{\partial t} + \frac{1}{A}\frac{\partial\left[A \alpha_k \rho_k u_k\left(h_k + \dfrac{u_k^2}{2 g_c J_c}\right)\right]}{\partial x} + \alpha_k \rho_k \frac{u_k}{g_c J_c} g \sin\theta - \dot{H}_k\right\} + \frac{\dot{Q}_{\text{loss}}}{A} = 0, \tag{D-12}$$

where J_c is another unit conversion factor, h_k is the enthalpy (BTU/lbm) of phase k (oil, water, or gas), $\dot{H}_k$ is the enthalpy influx per unit volume (BTU/ft^3·sec) of phase k, and $\dot{Q}_{\text{loss}}$ is the heat exchange per unit length (BTU/ft·sec) between the fluid and the surrounding environment. The latter is calculated by

$$\dot{Q}_{\text{loss}} = \pi D U\left(T - T_o\right), \tag{D-13}$$

where U is the overall heat-transfer coefficient (BTU/ft^2·sec·°F), T is the fluid temperature (°F), and T_o is the ambient temperature (°F).

The discretized version of this equation, for steady-state conditions, is then given by Eq. D-14:

$$\sum_{k=o,w,g}\left[(\rho_k\alpha_k u_k A)_{I+1}\left(h_{k_{I+1}}+\frac{u^2_{k_{I+1}}}{2g_cJ_c}\right)-(\rho_k\alpha_k u_k A)_I\left(h_{k_I}+\frac{(u_{k_I})^2}{2g_cJ_c}\right)\right] = V_{b_i}\sum_{k=o,w,g}\left(\dot{H}_{k_i}-\alpha_{k_i}\rho_{k_i}\frac{u_{k_i}}{g_cJ_c}g\sin\theta_i\right)-\Delta x_i\dot{Q}_{\text{loss}_i}. \tag{D-14}$$

Flow Regime. For steady-state simulations, no slip is assumed between oil and water phases, which have their properties averaged to form a liquid phase. Liquid/gas slip then comes from specific correlations for each flow regime. In general, parameters such as inclination, phase velocity, density, and viscosity are used to determine the flow pattern corresponding to each gridblock.

Currently, UTWELL uses models by Hasan et al. (2007), Kaya et al. (1999), and Taitel et al. (1980) for the vertical flow regimes (**Fig. D-2**). For horizontal flow, models from Shoham (2006) and Taitel and Dukler (1976) are implemented (**Fig. D-3**).

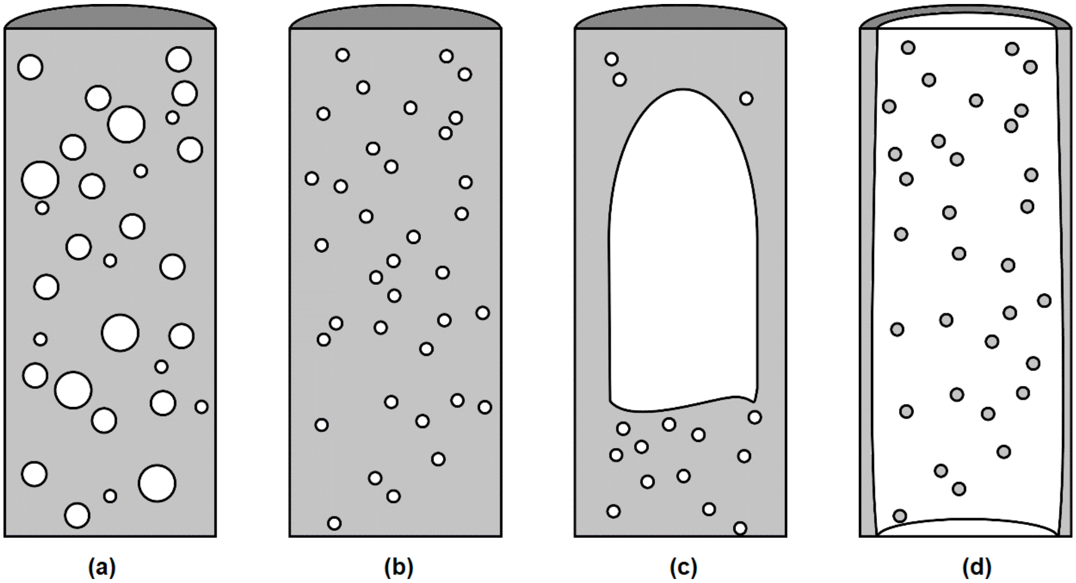

Fig. D-2—Schematic view of the vertical flow regimes: (a) bubbly flow, (b) dispersed bubbly flow, (c) slug flow, and (d) annular flow.

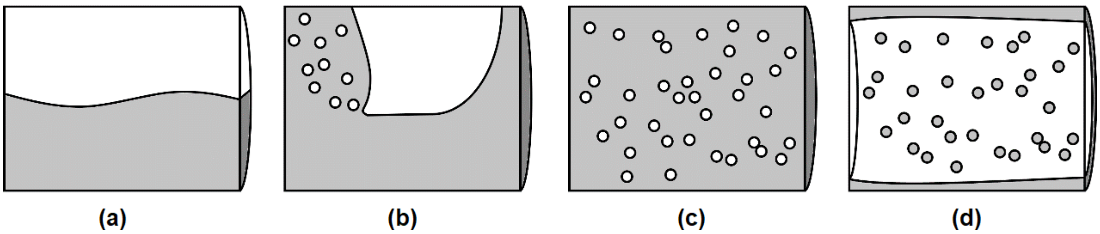

Fig. D-3—Schematic view of the horizontal flow regimes: (a) stratified flow, (b) slug flow, (c) dispersed bubbly flow, and (d) annular flow.

Numerical Method. In UTWELL, the steady-state module uses a marching algorithm to solve the flow equations. In this approach, all parameters are calculated iteratively from inlet to outlet until convergence is achieved for the entire domain. There are two convergence criteria: one related to the equations for an individual gridblock and another to the boundary conditions.

Initially, if pressure is not imposed by the inlet boundary condition, a value close to the reservoir pressure is guessed for the first gridblock. Then, mass conservation (Eqs. D-1 through D-3) is solved, so that the phase velocities are known. Using momentum conservation (Eq. D-11) and the flow-regime correlations, pressure drop and liquid holdup are also calculated. Next, energy conservation (Eq. D-14) is solved iteratively to obtain the corresponding temperature. Once convergence is achieved across all the conservation equations for the first gridblock, a pressure gradient can now be estimated and then used to update the pressure of the next node.

The entire process is repeated until all the gridblocks have been addressed. If a boundary condition such as constant wellhead pressure or flow rate was imposed at the outlet, the calculated values must be compared with those. In case they are not close enough, a new inlet pressure is guessed and the entire process is restarted until the algorithm achieves overall convergence.

Particle Deposition. In this section we introduce the basic terminology and equations used in the deposition models. Despite having other models available in UTWELL (Shirdel et al. 2012), only one (Escobedo and Mansoori 1995) is described here.

Terminology. The global mass transfer coefficient of particles moving towards the wall is given by

$$K_t=\frac{\dot{m}_t}{C_b-C_s}, \tag{D-15}$$

where $\dot{m}_t$ is the total mass flux and $(C_b - C_s)$ is the concentration difference between the average bulk flow and the surface. Still, K_t can be written in nondimensional form:

$$K_t^+ = \frac{K_t}{V_{\mathrm{avg}}\sqrt{f/2}}, \tag{D-16}$$

where $V_{\mathrm{avg}}\sqrt{f/2}$ is the fluid average velocity (Epstein 1988).

If we assume that a spherical particle moves with initial velocity V_p in a viscous fluid, the distance in which the particle stops due to drag forces is called the Stokes stopping distance S_p. After solving the force balance on the particle, we obtain

$$S_p = \frac{V_p \rho_p d_p^2}{18\mu}, \tag{D-17}$$

where ρ_p and d_d are the particle density and diameter, respectively, and μ is the fluid viscosity. V_p is approximated according to Friedlander and Johnstone (1957) by

$$V_p = 0.9\ V_{\mathrm{avg}}\sqrt{f/2}. \tag{D-18}$$

The nondimensional stopping distance is given by

$$S_p^+ = S_p \frac{\rho V_{\mathrm{avg}}\sqrt{f/2}}{\mu}. \tag{D-19}$$

The relaxation time, a characteristic value, is calculated by

$$t_p = \frac{S_p}{V_p} = \frac{\rho_p d_p^2}{18\mu}, \tag{D-20}$$

and in nondimensional form:

$$t_p^+ = t_p \frac{\rho V_{\mathrm{avg}}^2 \left(f/2\right)}{\mu}. \tag{D-21}$$

Other terms that are used in the deposition rate equations are the Brownian diffusivity and Schmidt number. Assuming a dilute suspension of spheres and no-slip condition on the surface of the spheres, the Brownian diffusivity is obtained from the Stokes-Einstein equation (Bird et al. 2002) as follows:

$$D_B = \frac{K_B T}{3\pi\mu d_p}, \tag{D-22}$$

where K_B is the Boltzmann constant.

The Schmidt number can be calculated as

$$\mathrm{Sc} = \frac{\mu}{\rho D_B}. \tag{D-23}$$

Deposition Mechanisms. There are three main mechanisms for particle deposition. Depending on the relaxation time, one of the mechanisms becomes dominant. We define these mechanisms as diffusion ($t_p^+ < 0.1$), inertia ($0.1 < t_p^+ < 10$), and impaction ($t_p^+ > 10$).

The diffusion mechanism becomes dominant for small particles (usually, less than 1 μm), with small stopping distances. In this case, Brownian motion carries particles to the wall. By increasing particles' size, the inertia effect takes place in the deposition process. In this mechanism, particles can obtain sufficient momentum by turbulent eddies to reach the wall. Finally, for large particle size ($t_p^+ > 10$), the impaction mechanism is dominant; the stopping distance is in the same order as the pipe diameter, and the particles no longer respond to the turbulent flow eddies.

Escobedo and Mansoori (1995)**.** The equations for the transport coefficient are presented as follows.

$0 < S_p^+ \leq 5$: stopping distance is located in the sublaminar layer

$$\begin{aligned} K_t^+ = \Bigg[& \frac{11.15\ \mathrm{Sc}^{2/3}}{3} F_1\left(\mathrm{Sc}, S_p^+\right) - \frac{\left(11.15\right)^2\ \mathrm{Sc}^{1/3}}{1.5\ D^+} F_2\left(\mathrm{Sc}, S_p^+\right) + 11.4\left(\frac{\mathrm{Sc}}{0.049774\ \mathrm{Sc} - 1}\right)^{1/2} F_3\left(\mathrm{Sc}\right) \\ & - \frac{\left(11.4\right)^2}{D^+} \ln\left(\frac{1 - 0.049774\ \mathrm{Sc} + \left(\frac{30}{11.4}\right)^2 \mathrm{Sc}}{1 - 0.049774\ \mathrm{Sc} + \left(\frac{5}{11.4}\right)^2 \mathrm{Sc}}\right) + \left(2.5 + \frac{12.5}{D^+ \mathrm{Sc}}\right) \ln\left(\frac{1 + 0.4\ r_{\mathrm{avg}}^+\ \mathrm{Sc}}{1 + 12\ \mathrm{Sc}}\right) - \frac{5\left(r_{\mathrm{avg}}^+ - 30\right)}{D^+} \Bigg]^{-1}, \end{aligned} \tag{D-24}$$

where

$$F_1\left(\mathrm{Sc}, S_p^+\right) = \frac{1}{2}\ln\left[\frac{\left(1+\frac{5}{11.15}\mathrm{Sc}^{1/3}\right)^2}{1-\frac{5}{11.15}\mathrm{Sc}^{1/3}+\left(\frac{5}{11.15}\right)^2\mathrm{Sc}^{2/3}}\right] - \frac{1}{2}\ln\left[\frac{\left(1+\frac{S_p^+}{11.15}\mathrm{Sc}^{1/3}\right)^2}{1-\frac{S_p^+}{11.15}\mathrm{Sc}^{1/3}+\left(\frac{S_p^+}{11.15}\right)^2\mathrm{Sc}^{2/3}}\right] + \sqrt{3}\,\tan^{-1}\left[\frac{\left(\frac{10}{11.15}\right)\mathrm{Sc}^{1/3}-1}{\sqrt{3}}\right] - \sqrt{3}\,\tan^{-1}\left[\frac{\left(\frac{2\,S_p^+}{11.15}\right)\mathrm{Sc}^{1/3}-1}{\sqrt{3}}\right], \tag{D-25}$$

$$F_2\left(\mathrm{Sc}, S_p^+\right) = \frac{1}{2}\ln\left[\frac{1-\frac{5}{11.15}\mathrm{Sc}^{1/3}+\left(\frac{5}{11.15}\right)^2\mathrm{Sc}^{2/3}}{\left(1+\frac{5}{11.15}\mathrm{Sc}^{1/3}\right)^2}\right] - \frac{1}{2}\ln\left[\frac{1-\frac{S_p^+}{11.15}\mathrm{Sc}^{1/3}+\left(\frac{S_p^+}{11.15}\right)^2\mathrm{Sc}^{2/3}}{\left(1+\frac{S_p^+}{11.15}\mathrm{Sc}^{1/3}\right)^2}\right] + \sqrt{3}\,\tan^{-1}\left[\frac{\left(\frac{10}{11.15}\right)\mathrm{Sc}^{1/3}-1}{\sqrt{3}}\right] - \sqrt{3}\,\tan^{-1}\left[\frac{\left(\frac{2\,S_p^+}{11.15}\right)\mathrm{Sc}^{1/3}-1}{\sqrt{3}}\right], \tag{D-26}$$

$$F_3\left(\mathrm{Sc}\right) = \frac{1}{2}\ln\left[\frac{\sqrt{0.049774\,\mathrm{Sc}-1}-\left(\frac{30}{11.4}\right)\mathrm{Sc}^{1/2}}{\sqrt{0.049774\,\mathrm{Sc}-1}+\left(\frac{30}{11.4}\right)\mathrm{Sc}^{1/2}}\right] - \frac{1}{2}\ln\left[\frac{\sqrt{0.049774\,\mathrm{Sc}-1}-\left(\frac{5}{11.4}\right)\mathrm{Sc}^{1/2}}{\sqrt{0.049774\,\mathrm{Sc}-1}+\left(\frac{5}{11.4}\right)\mathrm{Sc}^{1/2}}\right], \tag{D-27}$$

and D^+ is the nondimensional pipe diameter, given by

$$D^+ = D\frac{\rho V_{\mathrm{avg}}\sqrt{f/2}}{\mu}, \tag{D-28}$$

and r^+_{avg} is the nondimensional form of r_{avg}, the radial distance from the wall to the point where the fluid velocity is equal to the average velocity ($u = V_{\mathrm{avg}}$). This parameter is calculated as follows:

$$r^+_{\mathrm{avg}} = r_{\mathrm{avg}}\frac{\rho V_{\mathrm{avg}}\sqrt{f/2}}{\mu}, \tag{D-29}$$

$5 < S_p^+ \le 30$: stopping distance is located in the buffer zone

$$K_t^+ = \left[11.4\left(\frac{\mathrm{Sc}}{0.049774\,\mathrm{Sc}-1}\right)^{1/2} F_3\left(\mathrm{Sc}\right) - \frac{\left(11.4\right)^2}{D^+}\ln\left(\frac{1-0.049774\,\mathrm{Sc}+\left(\frac{30}{11.4}\right)^2\mathrm{Sc}}{1-0.049774\,\mathrm{Sc}+\left(\frac{S_p^+}{11.4}\right)^2\mathrm{Sc}}\right) + \left(2.5+\frac{12.5}{D^+\mathrm{Sc}}\right)\ln\left(\frac{1+0.4\,r^+_{\mathrm{avg}}\,\mathrm{Sc}}{1+12\,\mathrm{Sc}}\right) - \frac{5\left(r^+_{\mathrm{avg}}-30\right)}{D^+}\right]^{-1}, \tag{D-30}$$

$S_p^+ > 30$: stopping distance is located in the turbulent core

$$K_t^+ = \left[\left(2.5+\frac{12.5}{D^+\mathrm{Sc}}\right)\ln\left(\frac{1+0.4\,r^+_{\mathrm{avg}}\,\mathrm{Sc}}{1+0.4\,S_p^+\,\mathrm{Sc}}\right) - \frac{5\left(r^+_{\mathrm{avg}}-S_p^+\right)}{D^+}\right]^{-1}. \tag{D-31}$$

Attachment Process. Several active forces between the particles and the fluid, as well as between the particles and the wall, influence the deposition process. The source of those forces can be electrostatic and polar attractions, or the shear forces due to high velocity and viscosity of the flow. For gas systems, since shear forces are not significant, detachment of the particles is not pronounced. However, for liquid systems, those forces are very important. One approach to include the attachment process is applying a sticking probability function to the final transport coefficient, where the deposition coefficient could be modified as

$$K_D = SP\,K_t, \tag{D-32}$$

where the sticking probability (SP) is defined by Watkinson and Epstein (1970) as

$$SP = k_d \frac{e^{-E_a/RT}}{V_{\text{avg}}^2}, \qquad \text{(D-33)}$$

where k_d and E_a are experimentally regressed parameters.

The deposited particle mass flux is then given by

$$\dot{m}_d = K_D \left(C_b - C_s \right), \qquad \text{(D-34)}$$

where C_s is assumed zero.

The deposited solid can still be removed from the wall due to shear forces. For this, we define the deposit removal rate as

$$\frac{d\delta}{dt} = k_r \delta \tau^a, \qquad \text{(D-35)}$$

where k_r and a are regressed parameters.